MIT Open Access Articles

Antarctic sea ice control on the depth of North Atlantic deep water

The MIT Faculty has made this article openly available. ***Please share*** how this access benefits you. Your story matters.

Citation	Nadeau, Louis-Philippe, Raffaele Ferrari, and Malte F. Jansen, "Antarctic sea ice control on the depth of North Atlantic deep water." Journal of climate 32, 9 (May 2019): p. 2537-51 doi 10.1175/JCLI-D-18-0519.1 ©2019 Author(s)
As Published	10.1175/JCLI-D-18-0519.1
Publisher	American Meteorological Society
Version	Final published version
Citable link	https://hdl.handle.net/1721.1/124619
Terms of Use	Article is made available in accordance with the publisher's policy and may be subject to US copyright law. Please refer to the publisher's site for terms of use.

Massachusetts Institute of Technology

DSpace@MIT

Antarctic Sea Ice Control on the Depth of North Atlantic Deep Water

LOUIS-PHILIPPE NADEAU

Institut des Sciences de la Mer de Rimouski, Université du Québec à Rimouski, Rimouski, Quebec, Canada

RAFFAELE FERRARI

Department of Earth, Atmospheric, and Planetary Sciences, Massachusetts Institute of Technology, Cambridge, Massachusetts

MALTE F. JANSEN

Department of the Geophysical Sciences, University of Chicago, Chicago, Illinois

(Manuscript received 13 August 2018, in final form 24 January 2019)

ABSTRACT

Changes in deep-ocean circulation and stratification have been argued to contribute to climatic shifts between glacial and interglacial climates by affecting the atmospheric carbon dioxide concentrations. It has been recently proposed that such changes are associated with variations in Antarctic sea ice through two possible mechanisms: an increased latitudinal extent of Antarctic sea ice and an increased rate of Antarctic sea ice formation. Both mechanisms lead to an upward shift of the Atlantic meridional overturning circulation (AMOC) above depths where diapycnal mixing is strong (above 2000 m), thus decoupling the AMOC from the abyssal overturning circulation. Here, these two hypotheses are tested using a series of idealized two-basin ocean simulations. To investigate independently the effect of an increased latitudinal ice extent from the effect of an increased ice formation rate, sea ice is parameterized as a latitude strip over which the buoyancy flux is negative. The results suggest that both mechanisms can effectively decouple the two cells of the meridional overturning circulation (MOC), and that their effects are additive. To illustrate the role of Antarctic sea ice in decoupling the AMOC and the abyssal overturning cell, the age of deep-water masses is estimated. An increase in both the sea ice extent and its formation rate yields a dramatic "aging" of deep-water masses if the sea ice is thick and acts as a lid, suppressing air–sea fluxes. The key role of vertical mixing is highlighted by comparing results using different profiles of vertical diffusivity. The implications of an increase in water mass ages for storing carbon in the deep ocean are discussed.

1. Introduction

Proxy data of the Last Glacial Maximum (LGM) suggest that the rate of formation and depth of North Atlantic Deep Water (NADW) were considerably weaker and shallower than they are today (e.g., Curry and Oppo 2005; Lynch-Stieglitz et al. 2007; Burke et al. 2015). In contrast deep waters of Antarctic origins, which fill the global ocean below 3000 m in the present-day climate, extended above 2000 m during the LGM (Curry and Oppo 2005). Data further suggest a strong increase in abyssal stratification[1] (e.g., Adkins et al. 2002; Roberts et al. 2016), along with a reduction in the mixing between waters of North Atlantic and of Antarctic origin (Lund et al. 2011). It has been argued that these rearrangements in ocean circulation and stratification contributed to the large variations in atmospheric carbon dioxide concentration observed between glacial and interglacial periods—the ocean is the largest reservoir of carbon that can interact with the atmosphere on those time scales (e.g., Broecker 1982; Toggweiler 1999; Brovkin et al. 2007; Adkins 2013).

Most hypotheses for explaining the changes in deep-ocean stratification and circulation between glacial and interglacial periods have focused on changes in North Atlantic convection and shifts in Southern Hemisphere westerlies (e.g., de Boer et al. 2007; Toggweiler 2009; Anderson et al. 2009). However, increasing attention has been given to the potential role of buoyancy fluxes and sea ice at the surface of the Southern Ocean (e.g.,

[1] Notice, however, that the interpretation of these data has been questioned in some recent studies (e.g., Miller et al. 2015; Wunsch 2016a,b).

Corresponding author: Louis-Philippe Nadeau, louis-philippe_nadeau@uqar.ca

DOI: 10.1175/JCLI-D-18-0519.1

© 2019 American Meteorological Society. For information regarding reuse of this content and general copyright information, consult the AMS Copyright Policy (www.ametsoc.org/PUBSReuseLicenses).

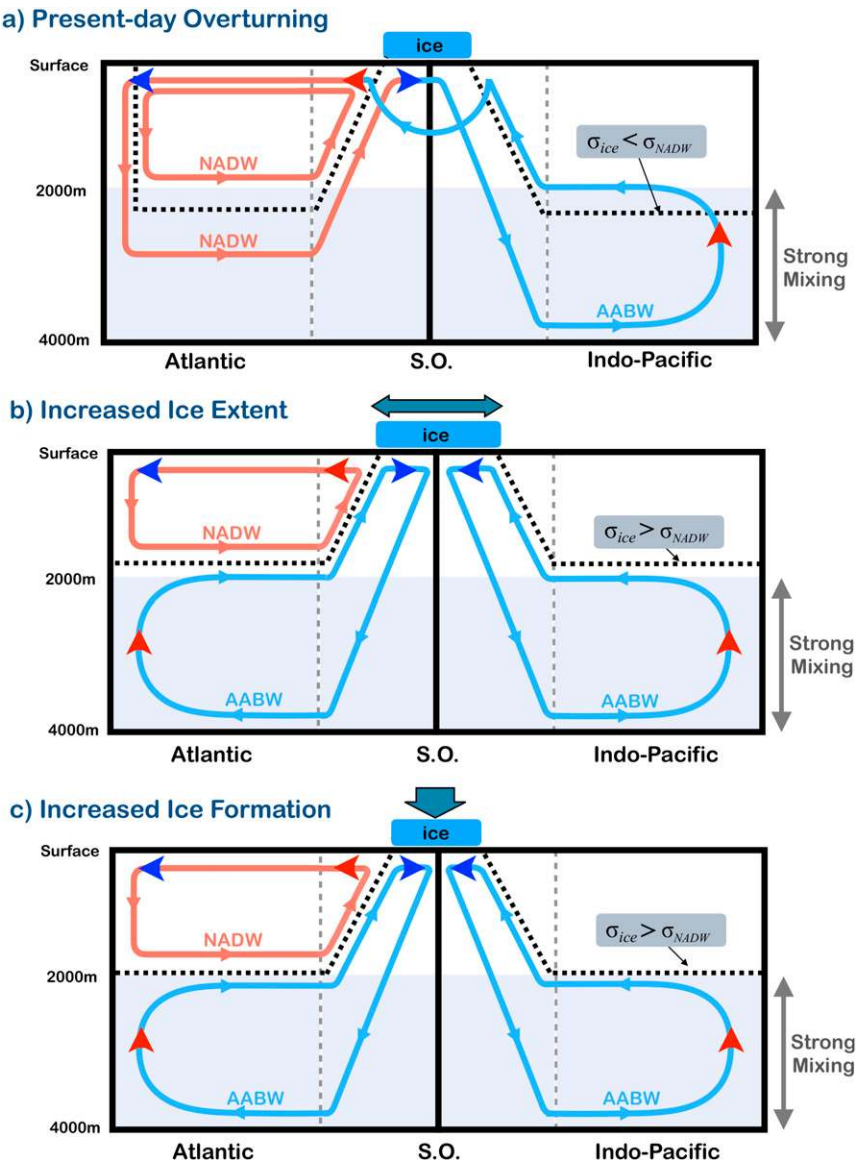

FIG. 1. Schematic of the meridional overturning circulation for (a) the present-day climate, (b) increased permanent Antarctic sea ice extent, and (c) increased Antarctic sea ice formation rate. Water masses belonging to the upper cell are represented by red lines, whereas those belonging to the abyssal cell are represented by blue lines. Red and blue arrows represent water mass transformation (lighter and denser, respectively) occurring through surface fluxes in the mixed layer or through diapycnal mixing in the ocean interior. In each panel, the isopycnal outcropping at the ice edge σ_{ice} is represented by a black dashed line. The deepest density class of NADW is referred to as σ_{NADW}.

Shin et al. 2003; Liu et al. 2005; Adkins 2013; Ferrari et al. 2014; Sun et al. 2016; Jansen and Nadeau 2016; Watson et al. 2015; Roberts et al. 2016; Jansen 2017). In particular, we recently made a case for the role of Antarctic sea ice through two main mechanisms: (i) increased latitudinal extent of permanent Antarctic sea ice (Ferrari et al. 2014) and (ii) increased rate of Antarctic sea ice formation (Jansen and Nadeau 2016). Both mechanisms result in a shoaling of NADW and an expansion of the abyssal waters of Antarctic origin.

The potential role of Antarctic sea ice on the global circulation is illustrated in Fig. 1. Each panel shows a latitude–depth schematic of the meridional overturning circulation (MOC) spanning the Southern Ocean (central region of the schematic between the vertical dashed gray lines), the Atlantic Ocean (left side of the schematic)

and the Indo-Pacific Ocean (right side of the schematic). The main pathways of the present-day MOC are sketched in Fig. 1a. Ferrari et al. (2014) argued that the permanent (summer) Antarctic sea ice, shown as a blue rectangle, is strongly linked to the pathways of the MOC by controlling, on average, the transition from negative to positive buoyancy fluxes at the surface of the Southern Ocean. The lower branch of NADW, with density $\sigma \sim \sigma_{\mathrm{NADW}}$, upwells under the Antarctic sea ice cover. Exposed to negative buoyancy fluxes (blue arrow under ice), this water mass is transformed into Antarctic Bottom Water (AABW), fueling the abyssal cell of the MOC (e.g., Talley 2013; Abernathey et al. 2016). The upper branch of the NADW that upwells north of the sea ice is instead exposed to positive buoyancy fluxes (red arrow north of the ice) and is transformed into Antarctic Intermediate and Subantarctic Mode Waters as part of the middepth cell of the MOC (e.g., Talley 2013). The isopycnal outcropping at the permanent sea ice edge has a density σ_{ice} less than σ_{NADW} and marks the division between the two branches of the NADW. At the northern end of the Drake Passage, the depth of σ_{ice} depends on both the isopycnal slope and the latitudinal distance to the sea ice edge. In this present-day overturning, the zonally averaged permanent sea ice edge is very close to Antarctica, and σ_{ice} plunges deep before reaching the latitudes of the Atlantic and Indo-Pacific basins. At those depths (below ~2000 m), strong vertical mixing allows for AABW to diffuse into density classes occupied by NADW (red arrow across σ_{ice} in the Indo-Pacific). Thus, mixing inherently allows for the overlapping and coupling between the Atlantic middepth cell (lower branch of the NADW) and the Indo-Pacific abyssal cell.

The hypothesis of Ferrari et al. (2014), sketched in Fig. 1b, relies on a geometric argument. Assuming a constant isopycnal slope in the channel,[2] an increased permanent sea ice latitudinal extent during the LGM would lead to a northward shift of the isopycnal outcropping at the permanent sea ice edge and a shoaling of the depth at which it connects to the basins to the north. If this shoaling reaches a region of weak mixing (above ~2000 m), it is no longer possible for AABW to upwell diffusively into a density class that outcrops north of the ice line. Exposed to negative buoyancy fluxes at the surface, these waters must be transformed back to AABW and the abyssal overturning thus closes on itself. By mass continuity, the upper cell must also close on itself and be confined to buoyancy classes outcropping north of the ice line ($\sigma_{\mathrm{NADW}} < \sigma_{\mathrm{ice}}$), thus shoaling the NADW. As the overlap between the cells vanishes, the water masses of the middepth cell get increasingly isolated from those of the abyssal cell.

The hypothesis of Jansen and Nadeau (2016), sketched in Fig. 1c, relies on basin thermodynamics. An increase in the formation rate of sea ice results in a larger buoyancy loss under sea ice through brine rejection. This loss is balanced by a larger buoyancy gain through ice melting farther north, but the latter affects only the formation of intermediate and mode waters. The abyssal overturning cell only experiences the increased buoyancy loss under sea ice, which must be balanced by increased buoyancy gain through mixing with waters of the middepth cell. For a given vertical diffusivity profile, this requires increased stratification. Since the upper-ocean density remains largely unaffected, the increased stratification in turn is associated with higher densities in the abyssal cell. As a result, σ_{ice} becomes denser than σ_{NADW}, and the upper cell becomes confined to shallower depths (above the σ_{ice} isopycnal). As in the sea ice expansion scenario, the two cells end up closing on themselves thus isolating the two water masses.

The goal of this study is to better understand both the impact of Antarctic permanent sea ice latitudinal extent and formation rate on rearranging the deep-ocean water masses in a two-basin ocean general circulation model (OGCM). During glacial climates, it is likely that both the extent and formation rate of permanent sea ice increased (e.g., Gersonde et al. 2005; Roche 2012; Adkins 2013). Rather than attempting a quantitative reconstruction of the LGM ocean circulation, we want to qualitatively understand the impact of changes in permanent Antarctic sea ice on the depth of NADW and ventilation of the abyssal ocean. Jansen and Nadeau (2016) studied both mechanisms using an OGCM in an idealized single-basin configuration. Their results highlighted the role of the integrated buoyancy loss rate in controlling the circulation and stratification. Here, we demonstrate that the effect of permanent sea ice extent can be of similar magnitude as the integrated buoyancy loss rate in a setup with two basins and a vertical diffusivity profile that represents the large increase in turbulent mixing below about 2000 m (the depth extent of midocean ridges and seamounts) and that the two effects are additive.

The manuscript is organized as follows. The numerical model is introduced in section 2, followed by a description of a reference present-day simulation in section 3. In section 4 we illustrate that an increase in permanent sea ice extent and integrated buoyancy loss rate lead to the same qualitative response in circulation: a shoaling of NADW

[2] The isopycnal slope results from a balance between the wind stress and an eddy-induced stress. Recent studies show that any increase in the wind stress triggers an increase in eddy activity such that the balance between the wind and eddy stresses results in very small change in isopycnal slope (e.g., Hallberg and Gnanadesikan 2006; Munday et al. 2013).

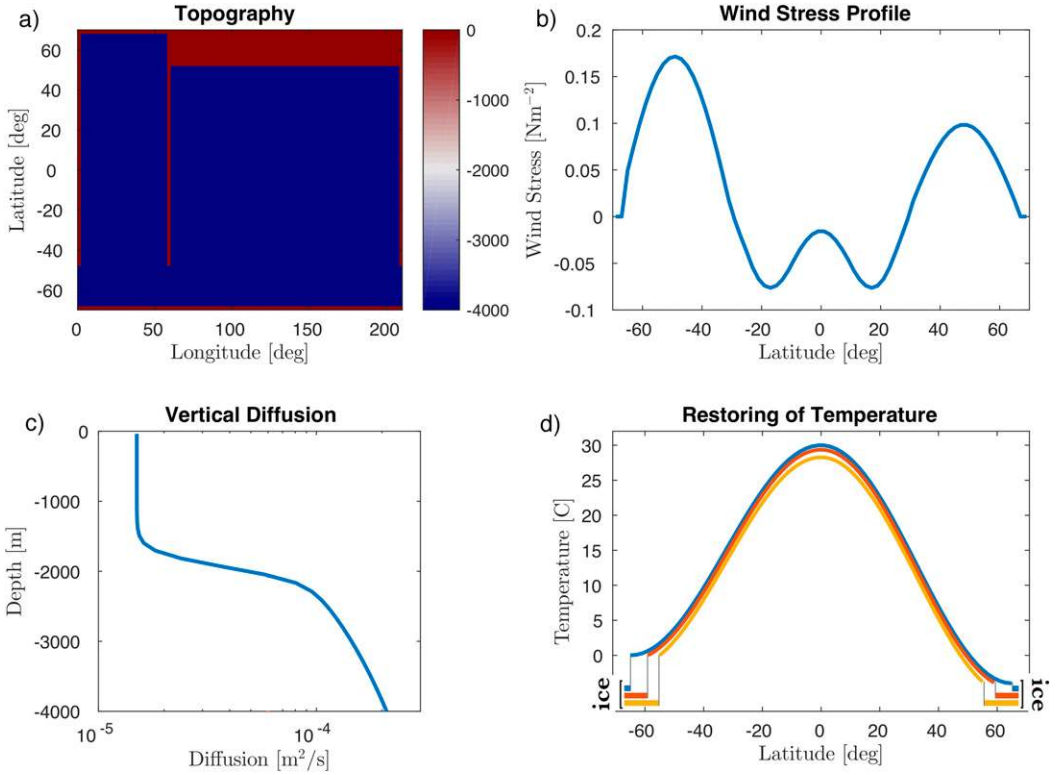

FIG. 2. Model configuration for the reference experiment: (a) model topography, (b) latitudinal profile of surface wind stress, (c) vertical profile of vertical diffusivity, and (d) latitudinal profile of temperature restoring for ice extents of 2° (blue), 8° (red), and 16° (yellow). The horizontal "ice" lines in (d) represent regions where a constant buoyancy flux is applied instead of restoring.

and a reduction of the overlap between the two cells of the MOC. The impact on the ventilation of the abyss is then estimated in section 5 using an age tracer. A significant reduction of the ventilation rate of the deep ocean is observed only if the permanent sea ice acts as a solid lid limiting air–sea exchanges, but not if the presence of polynyas and leads renders the sea ice effectively permeable. The key role of vertical mixing is investigated in section 6. Conclusions and implications for carbon storage are discussed in section 7.

2. Numerical models and experiment design

Numerical simulations are performed using an idealized configuration of the Massachusetts Institute of Technology General Circulation Model (MITgcm; Marshall et al. 1997). The model solves the hydrostatic Boussinesq equations on a spherical grid with a 2° horizontal resolution and 40 vertical levels with thickness increasing from 37 m at the surface to 159 m at the bottom. To eliminate potential complications due to the combined effect of temperature and salt on density, we use a linear equation of state that depends only on temperature, $\rho = \rho_0(1 - \alpha_\theta \theta')$, with a constant thermal expansion coefficient $\alpha_\theta = 2.0 \times 10^{-4}\,\mathrm{K}^{-1}$. Hence temperature is linearly proportional to density in the numerical simulations. Slumping of isopycnals through baroclinic instability at the mesoscale is parameterized as a layer thickness diffusion following Gent and McWilliams (1990) with a constant eddy diffusivity $\kappa_{\mathrm{GM}} = 1000\,\mathrm{m^2\,s^{-1}}$. To avoid unrealistically large passive tracer gradients, which otherwise develop at the surface of the Southern Ocean, the isopycnal diffusion is set to a higher value of $\kappa_{\mathrm{redi}} = 3000\,\mathrm{m^2\,s^{-1}}$, still within the observational range (Balwada et al. 2016). Advection of temperature is achieved through a second-order moment superbee flux limiter scheme (Roe 1986). Ocean convection is represented as a convective adjustment, implemented as an enhanced vertical diffusivity of temperature.

The model's geometry is shown in Fig. 2. It consists of two basins connected to the south by a circumpolar channel. The domain covers 210° in longitude, extends from 70°S to 70°N in latitude, and is 4 km deep. The narrower Atlantic-like basin covers 60° in longitude. The wider Indo-Pacific-like basin is 150° wide and extends from 70°S to 54°N—a landmass occupies the latitudes between 54° and 70°N to mimic the reduced latitudinal extent of the North Pacific. The areas of the two basins correspond approximately to those of the

Atlantic and Indo-Pacific Oceans. The channel spans 20° in latitude and runs along the whole 210° of longitude. The model is forced at the surface by patterns of easterly and westerly winds broadly inspired by observations (Fig. 2b). To capture the transition from weak to large mixing sketched in Fig. 1, we impose a vertical diffusivity profile that is weak above 2000 m and increases exponentially downward in the bottom half of the water column (Fig. 2c). Values at the surface and the bottom are inspired by global estimates based on scaling laws for wave radiation and breaking applied to the global ocean (e.g., Nikurashin and Ferrari 2013).

The effect of permanent sea ice on the ocean is imposed as a negative buoyancy flux representing cooling and brine rejection (see Jansen and Nadeau 2016). This constant buoyancy loss per unit area is imposed over the latitude bands of extent l_{ice} at the northern and southern edges of the model domain, which we refer to as "ice strips." Notice that the integrated buoyancy loss under the southern ice strip is much larger than under the northern ice strip, since the buoyancy loss in the north is applied only over the zonal extent of the narrow basin, while the wider basin is covered by a landmass at high latitudes. Equatorward of these ice strips, temperature (buoyancy) is restored to a prescribed sinusoidal latitudinal profile going from 0°C at the southern sea ice edge to −4°C at the northern sea ice edge (Fig. 2d), with a piston velocity of about 1 m day^{-1}. The value of restoring at the equator depends on the value of l_{ice} (see Fig. 2d) and no restoring of temperature is applied under the ice strips. The colder restoring temperature in the north is applied to mimic the effect of salinity, which acts to increase the density of waters in the North Atlantic and is chosen to yield a 3000-m-deep NADW, similar to the present-day circulation. There is no seasonal cycle in the forcing and therefore the sea ice strips do not undergo seasonal contractions and expansions: all sea ice is by definition permanent in this model. While Jansen (2017) finds that this approach captures the key feedbacks of sea ice on the MOC, the reader should keep in mind that in our model sea ice acts only as a thermodynamic boundary condition.

This specific combination of restoring and flux of buoyancy allows us to investigate independently the effect of an increased sea ice extent from that of an increased sea ice formation rate. An increase in sea ice formation rate is represented as an increase in the integrated buoyancy loss rate $\mathcal{B}$ under a fixed ice extent l_{ice}. An increase in sea ice extent is instead represented as an increase in l_{ice} for a fixed $\mathcal{B}$. We will also combine both effects by varying the width and flux simultaneously. For presentation purposes, we choose to keep the temperature restoring at the southern ice edge at 0°C in all experiments, despite the fact that the 0°C temperature point is arbitrary in a Boussinesq model with no explicit sea ice (see Fig. 2d). Also for presentation purposes, we choose to express all integrated buoyancy fluxes in terms of the corresponding heat flux in terrawatts.

Our model configuration differs from that used in Jansen and Nadeau (2016) in two main respects, in addition to the inclusion of a second Indo-Pacific basin: (i) a second ice strip is added at the north of the narrow basin and (ii) the surface latitudinal buoyancy gradient is fixed away from the ice strips in all simulations. Compared to the inclusion of a second basin, these modifications appear to have only limited impacts on the results and will be briefly discussed in section 4.

3. Reference present-day simulation

To get started we illustrate the circulation that develops in a "reference" experiment (Fig. 3) designed to capture the main features of the global MOC in the present-day climate. This reference experiment is performed using an ice extent $l_{\text{ice}} = 2°$ in latitude (blue curve on Fig. 2) and an integrated buoyancy loss under ice $\mathcal{B} = 25$ TW (cf. Ferrari et al. 2014). The vertically integrated transport streamfunction ψ_{BT} (Fig. 3a) shows a typical pattern of horizontal circulation with a strong circumpolar current in the channel and weaker wind-driven gyres to the north in the closed basins.

Figure 3c shows the zonally integrated residual meridional circulation ψ_{res} in a latitude–depth plane. This residual streamfunction is defined as the vertically integrated meridional transport below a density surface,

$$\psi_{\text{res}}(y,\sigma) = -\frac{1}{T}\int_0^T\int_0^{L_\sigma}\int_{-H}^{h(x,y,\sigma,t)} v_{\text{res}}(x,y,z,t)\,dz\,dx\,dt, \qquad (1)$$

where $h(x, y, \sigma, t)$ is the depth of the isopycnal σ as a function of space and time, H is the total ocean depth, L_σ is the zonal length of the isopycnal σ at the latitude y, T is the period of the time average, and $v_{\text{res}} = v + v_{\text{GM}}$ is the total meridional velocity given by the sum of the resolved velocity v and the eddy-induced velocity v_{GM} [parameterized with the Gent and McWilliams (1990) closure]. The residual streamfunction is plotted as a function of the zonal and temporal mean depth of each isopycnal, $z_\sigma(\sigma, y) = -(1/TL_\sigma)\int_0^T\int_0^{L_\sigma} h(x, y, \sigma, t)\,dx\,dt$, in Figs. 3b–d. The residual circulation so defined captures the whole transport of tracers by mean, parameterized eddies, and correlations between velocities and heaving of isotherms. Time averages are performed over a period of $T = 500$ years at equilibrium,[3] which is

[3] In all experiments, the equilibrium is defined as the solution for which the area-averaged streamfunction becomes independent of time (i.e., no visible trend for the amplitude as a function of depth).

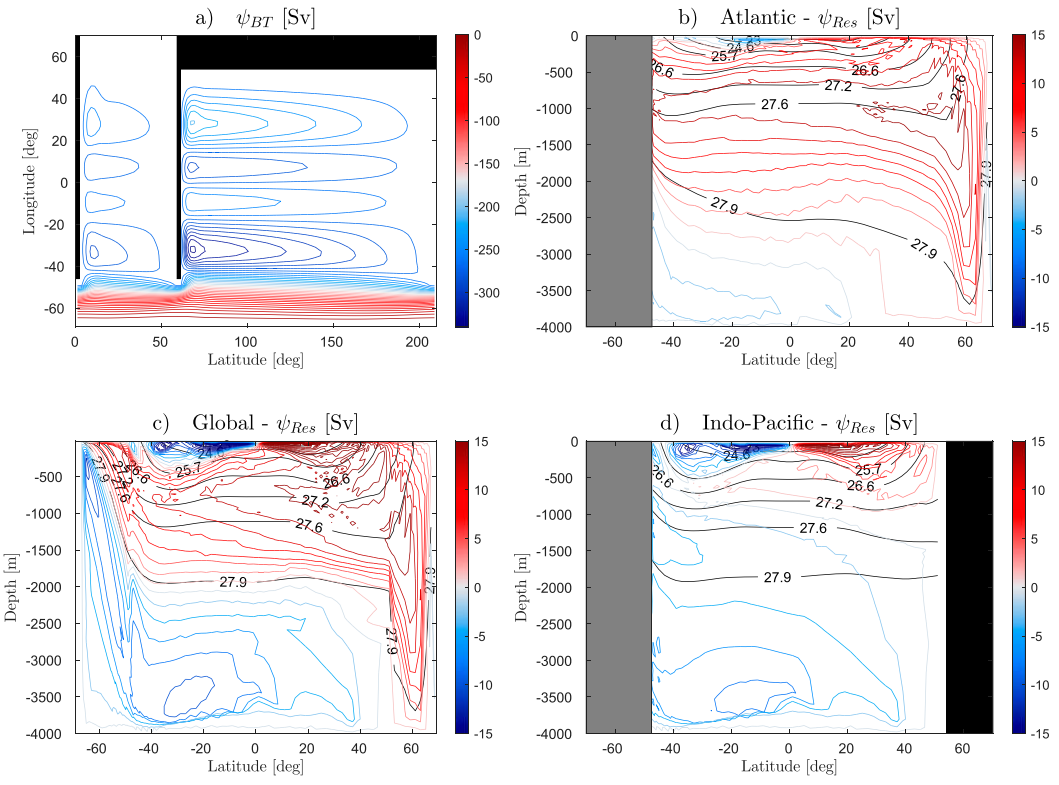

FIG. 3. Results for the reference present-day experiment: (a) vertically integrated transport streamfunction ψ_{BT} and (b)–(d) zonally integrated residual meridional streamfunction ψ_{res} computed over (b) the Atlantic basin, (c) the full zonal extent, and (d) the Indo-Pacific basin. Black contours in (b)–(d) show density (kg m^{-3}). Contour intervals are 10 Sv for ψ_{BT} and 2 Sv for ψ_{res}.

reached after ~10 000 years. The global MOC in Fig. 3c is qualitatively similar to the one derived from observations (e.g., Lumpkin and Speer 2007): two shallow wind-driven cells, symmetric about the equator, one middepth cell confined to the narrow Atlantic-like basin, and one abyssal cell spanning both basins. Figures 3b and 3d of the MOC for the narrow and wide basins separately show that the middepth cell is associated with waters sinking in the north and flowing southward at depth along isopycnals toward the channel. The abyssal cell, instead, upwells across isopycnals through diabatic mixing due to the bottom-enhanced profile of vertical diffusivity (see Fig. 2c). The middepth cell has a transport of 16 Sv (1 Sv $\equiv 10^6$ m^3 s^{-1}) while the abyssal one transports 11 Sv.

Figures 3b and 3d show that the Atlantic middepth cell and the Indo-Pacific abyssal cell overlap over a wide range of depths (roughly $-3000 < z < -1000$ m) and density classes (roughly $27 < \sigma < 28$ kg m^{-3}), similarly to the circulation sketched in Fig. 1a. In view of the fact that large-scale oceanic motions are primarily directed along density surfaces, this overlapping suggests a strong exchange of water, or coupling, between the two overturning cells. In the Southern Ocean, the separation between the cells at the surface occurs at the ice edge (Fig. 3c), where the surface buoyancy flux changes sign from a negative value under ice, to a positive value north of the ice. The position of the density surface that outcrops at the ice edge ($\sigma_{\mathrm{ice}} \approx 27.9$ kg m^{-3}) is key to the coupling of the two cells. At the northern edge of the Drake Passage, this surface density splits the NADW flowing southward in the middepth cell of the Atlantic basin into two. The portion of the model's NADW that lies above σ_{ice} flows southward at depths where mixing is weak (above 2000 m), upwells adiabatically in the channel, surfaces under positive buoyancy flux, and returns northward as part of the upper branch of the Atlantic middepth cell (similar to the upper branch of the NADW in Fig. 1a). On the other hand, two pathways are possible for the portion of the model's NADW that flows southward below σ_{ice} in the Atlantic. First, this water can upwell under negative buoyancy flux at the surface of the channel, get denser, and sink back into the abyss, feeding the model's AABW (lower branch of the NADW sketched in Fig. 1a). Strong vertical mixing then allows for the Indo-Pacific AABW to diffusively upwell (up to ~2000-m depth) back into density classes $\sigma < \sigma_{\mathrm{ice}}$ occupied by NADW, thus coupling the middepth and abyssal cells. A second pathway exists where NADW water flows directly into the

Indo-Pacific through a geostrophic interbasin exchange.[4] This second pathway yields a small recirculation visible at ~1500 m at the southern edge of the Indo-Pacific basin in Fig. 3d. For both pathways, mixing is key to coupling the two cells. Figure 3 suggests that about half of the model's NADW is coupled to the Indo-Pacific abyssal cell, with about two thirds of this water coupled via the first pathway and the remaining via the second pathway.

Our reference present-day simulation shares many characteristics with the circulation patterns observed in the real ocean. Through analysis of water mass properties, Talley (2013) pointed out that about half of the observed NADW is transformed into denser AABW once it upwells at the surface of the Southern Ocean. This buoyancy loss occurs mainly under Antarctic sea ice during the Southern Hemisphere winter (Abernathey et al. 2016). The first pathway described in our model simulation is thus likely to be dominant in the present-day ocean.

4. Antarctic sea ice control on the depth of the Atlantic middepth overturning cell

We test the influence of the permanent "sea ice" latitudinal extent and the rate of buoyancy loss on the overturning circulation. Starting from the reference simulation, we perform experiments where we increase either the latitudinal extent or the magnitude of the buoyancy loss or both. Circulations obtained from these experiments are shown in Fig. 4. The three columns, from left to right, show the MOC zonally averaged over the full domain, the Atlantic basin, and the Indo-Pacific basin, respectively.

Note that the MOC in the channel matches the MOC zonally integrated over both basins in the north, but not the MOC of each basin individually. In the examples in Figs. 1b and 1c where no water is exchanged between the Atlantic middepth and Pacific abyssal cells, the MOC in the channel matches only the Atlantic middepth cell in the upper 1500 m. However in the example in Fig. 1a where there is substantial exchange of waters between the two cells, the MOC in the channel does not match those in either basin. As such, it is useful to consider the zonally integrated MOC, even if our goal is to describe how the overturning is partitioned between the two basins.

A fourfold increase of the ice strip latitudinal extent from $l_{\text{ice}} = 2°$ to 8°, with the same constant area integrated buoyancy loss of $\mathcal{B} = 25$ TW as in the reference run, leads to a significant shoaling of the model's averaged Atlantic middepth cell depth (Fig. 4b). The Atlantic abyssal cell expands farther up as the middepth cell shoals, as predicted by the geometric argument of Ferrari et al. (2014) and sketched in Fig. 1b. The shoaling of the middepth cell in Fig. 4b, marked with a dashed gray line, is much greater in the Atlantic basin than in the global zonal average. The depth difference between the globally averaged interface and the Atlantic interface is more than a thousand meters in the reference case Fig. 4a, but it is only a few hundred meters in Fig. 4b. The depth of the diabatic overturning in the Pacific is instead weakly sensitive to the change in ice strip extent, because it is primarily constrained by the vertical diffusivity profile. Therefore, a given change in the zonally integrated overturning is accomplished through a much larger change in the Atlantic basin. This also suggests a shift in circulation regime consistent with the sketch in Fig. 1b. As the ice line extends north, the isopycnal separating the two cells moves upward in a region of weak mixing (above 2000 m) and effectively decouples (or reduces the overlap between) the two MOC cells, thus isolating the middepth and abyssal water masses. This suggests that important variations in the ventilation of the abyssal ocean can occur without large variations in the globally averaged MOC. To separate the role of the southern versus northern ice strips, we performed an additional experiment where only the southern ice strip was expanded. The results differ only marginally from the experiment in Fig. 4b, suggesting that the circulation changes are dominantly driven by the Antarctic sea ice strip, consistent with the argument of Ferrari et al. (2014).

Increasing the rate of buoyancy loss from $\mathcal{B} = 25$ to 100 TW, with fixed $l_{\text{ice}} = 2°$ ice strip extent, yields a similar effect on the MOC as an increase in ice latitudinal extent (Fig. 4c). An enhanced buoyancy loss rate (representative of increased sea ice formation) induces a shoaling of the middepth cell and a reduction of its overlap with the abyssal cell. Although the response of the circulation to increased $\mathcal{B}$ is similar to increased l_{ice}, the physical mechanisms driving the shoaling are quite different. Jansen and Nadeau (2016) argue that the shoaling is a result of a strong increase in the stratification at the cell interface (Fig. 4), which in turn is required to close the buoyancy budget of the abyssal cell. From an isopycnal zonal average perspective, the integrated buoyancy loss south of the ice edge must be balanced by a diffusive buoyancy flux at the top of the abyssal cell (in both basins). The stratification at the interface between the two zonally averaged cells thus scales as

$$\partial_z b|_{z_{\text{ice}}} \sim \kappa_v^{-1}\mathcal{B},$$

where z_{ice} is the depth of the isopycnal separating the two cells. Jansen and Nadeau (2016) verified that this

[4] The idea that some NADW flows directly into the Indo-Pacific dates to Broecker (1991) and was formalized more recently as a geostrophic interbasin current resulting from a partial compensation between wind and eddies in the Southern Ocean (e.g., Thompson et al. 2016; Jones and Cessi 2016; Ferrari et al. 2017). For simplicity, this pathway was not sketched in Fig. 1a.

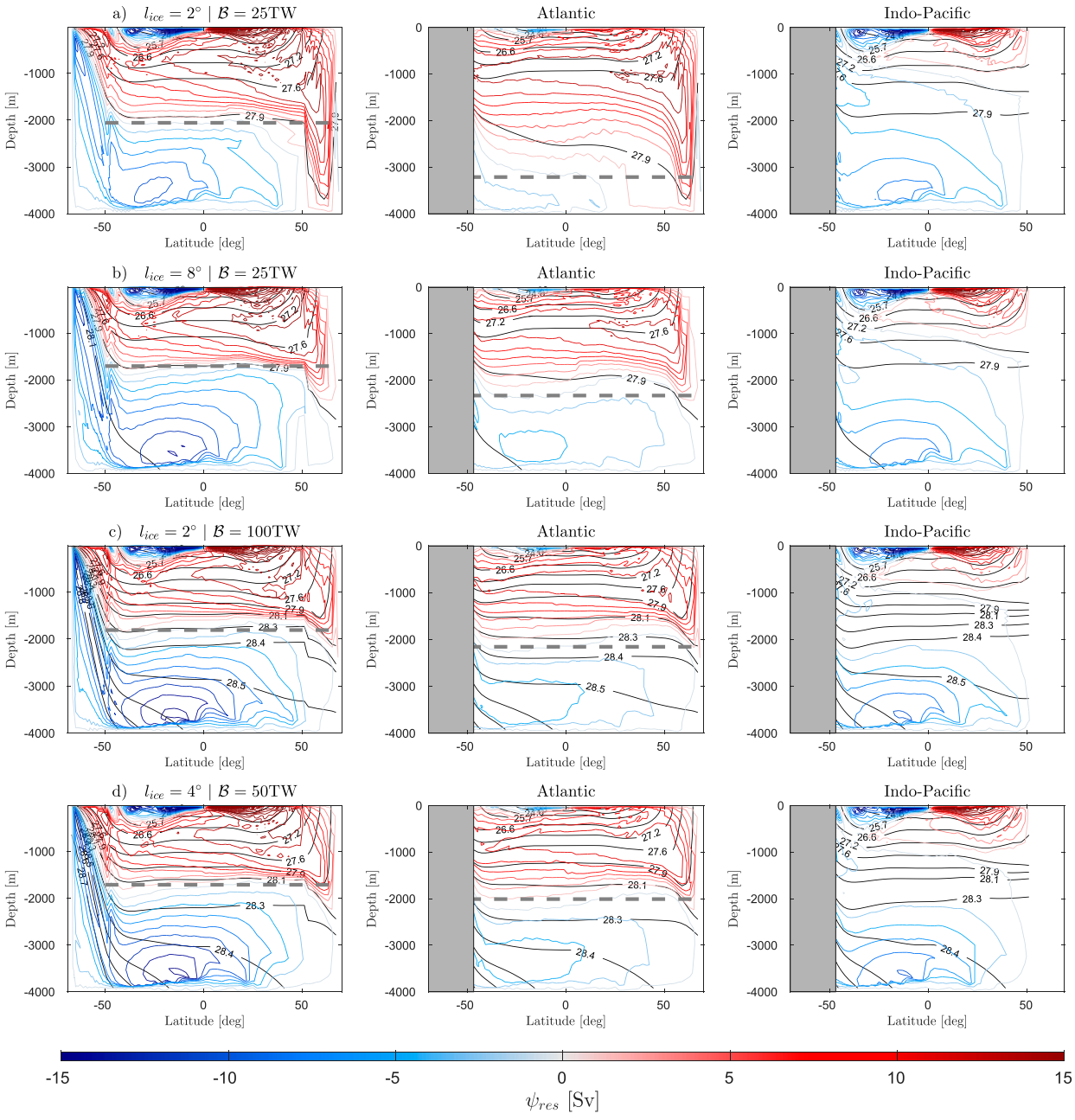

FIG. 4. Zonally integrated residual meridional streamfunction computed over (left) the full zonal extent, (center) the Atlantic basin, and (right) the Indo-Pacific basin. Each row corresponds to a different experiment: (a) reference case, (b) quadrupled l_{ice}, (c) quadrupled $\mathcal{B}$, and (d) doubled l_{ice} and $\mathcal{B}$. Black contours show density (kg m^{-3}). Dashed gray lines mark the interface between the middepth and abyssal cells computed between 50°S and 50°N. Contour interval for ψ_{res} is 2 Sv.

relationship holds to a good approximation in a single-basin configuration, but the theoretical argument applies as well to the zonal average of a two-basin configuration. Making the plausible assumption—supported by the numerical experiments—that the stratification in the upper ocean is approximately independent of changes in the buoyancy loss rate around Antarctica, the depth of the middepth cell can be found by estimating the depth at which $\partial_z b|z_{\text{ice}}$ matches the upper-ocean stratification. Given that the upper-ocean stratification is typically a decreasing function of depth, an increase in the abyssal stratification leads to a shoaling of the cell interface. The decreasing kappa toward the upper ocean requires an even larger change in stratification, thus amplifying the

shoaling. As in the case of increased ice extent, the shoaling in the zonal-mean depth of the interface is accomplished via a much larger shoaling of the middepth cell in the Atlantic basin, again leading to a strong reduction of the overlap between the two cells of the MOC.

The two illustrative scenarios considered above focused on extreme changes in l_{ice} and $\mathcal{B}$ to better illustrate the resulting changes in circulation. Figure 4d shows results from an experiment in which l and $\mathcal{B}$ have been increased simultaneously but more moderately, arguably a scenario more relevant to understand the LGM ocean circulation. Observational support exists for increased maximum and possibly permanent sea ice coverage (Gersonde et al. 2005; Roche 2012), as well as for an increase in abyssal Southern Ocean salinity (Adkins et al. 2002), which is most easily explained by increased brine rejection leading to larger buoyancy loss. Numerical simulations also suggest that both increased sea ice extent and increased sea ice formation occur simultaneously in a colder climate (e.g., Shin et al. 2003; Jansen 2017; Marzocchi and Jansen 2017). Starting from the reference simulation (Fig. 4a), doubling both l and $\mathcal{B}$ yields the same qualitative result as quadrupling each parameter independently. Notice however that the shoaling of the Atlantic middepth cell saturates for higher values of l and $\mathcal{B}$ (not shown), which is most likely due to the strongly varying diffusivity profile. Once the Atlantic middepth cell is confined to depths of weak vertical mixing, further increases in ice extent or formation rate have only a relatively weak effect.

5. Deep-water mass ages

We argued that the depth of the middepth cell plays a critical role in coupling the middepth and abyssal circulations and associated water masses. To quantify the effect of the circulation changes on deep-ocean ventilation, we introduce age tracers that quantify the time elapsed since a water mass was last in contact with the atmosphere.

An age tracer is a tracer that is advected by the full three-dimensional velocity field and ages by one year every year. Typically it satisfies no-flux conditions at solid boundaries and is reset to zero at the ocean surface. However it is not clear that the age tracer should be reset to zero in regions covered by sea ice, where gas exchange may be strongly inhibited. Here we will consider two age tracers satisfying different surface boundary conditions under the ice strips. The first age tracer will be restored to zero at the surface even under the ice strips, while the second age tracer will satisfy no-flux boundary conditions under the ice strips.

The first age tracer is appropriate to study the ventilation of deep-water masses, if the sea ice cover is sufficiently thin and brittle to be permeable to air–sea fluxes. In contrast the second age tracer tracks ventilation if the permanent sea ice is thick, without leads or polynyas, and thus inhibits any air–sea flux. Real tracers, like ^{14}C, will fall somewhere between these two extreme cases, both because the air–sea equilibration is not instantaneous even in the absence of any sea ice and because real sea ice is neither perfectly permeable nor completely insulating. It is also likely that there is a shift between the two cases with smaller ice concentrations (more permeable) for the present-day climate and larger ice concentrations (limiting air–sea exchanges) for colder climates.

The different boundary conditions for the two age tracers are imposed as follows: (i) rapid restoring to zero everywhere at the surface (piston velocity of about 40 m day^{-1}) and (ii) rapid restoring in the ice-free region, but no flux under the ice strips. Figures 5 and 6 show the distributions of the two age tracers for the various simulations.

Consider first the results for the reference present-day simulation, shown in the top row of in Figs. 5 and 6. In the basins the age distributions are pretty similar, the only difference being that a no-flux boundary condition leads to overall older water mass ages. The left panels show the depth-averaged tracer ages, with North Atlantic deep convection producing younger ages in the Atlantic than in the Indo-Pacific. An interbasin exchange of young waters from the eastern Atlantic basin to the western Indo-Pacific basin is seen in Fig. 5a. This leakage is a signature of the coupling between the Atlantic middepth cell and Indo-Pacific abyssal cell. The center and right panels show zonally averaged ages in the Atlantic and Indo-Pacific basins, respectively. In the Atlantic, ages increase from north to south, following the southward advection of NADW. In the Indo-Pacific there is a distinctive source of young waters from the south associated with the leakage of NADW from the Atlantic through the channel (particularly in the case with no flux under the ice strips in Fig. 5a). A similar signature of interbasin exchange is visible in the Atlantic, where a wedge of older Indo-Pacific waters can be seen at roughly 1000 m.

The two age tracer distributions are instead quite different in the channel region (top panels of Figs. 5 and 6). With a fast restoring under the ice strips, ages decrease toward Antarctica, resulting in a wedge of relatively old water connecting the surface of the channel at the ice edge to the abyss of each basins. With a no-flux condition under the ice strips, instead, ages increase from north to south. The Northern Hemisphere ice strip has almost no influence on the age tracers because the water that sinks in the North Atlantic is young regardless, being fed from the south by the young subpolar gyre always in contact with the atmosphere.

The two age tracers are very useful when it comes to diagnosing the degree of coupling and water mass exchanges between the middepth and abyssal cells in the

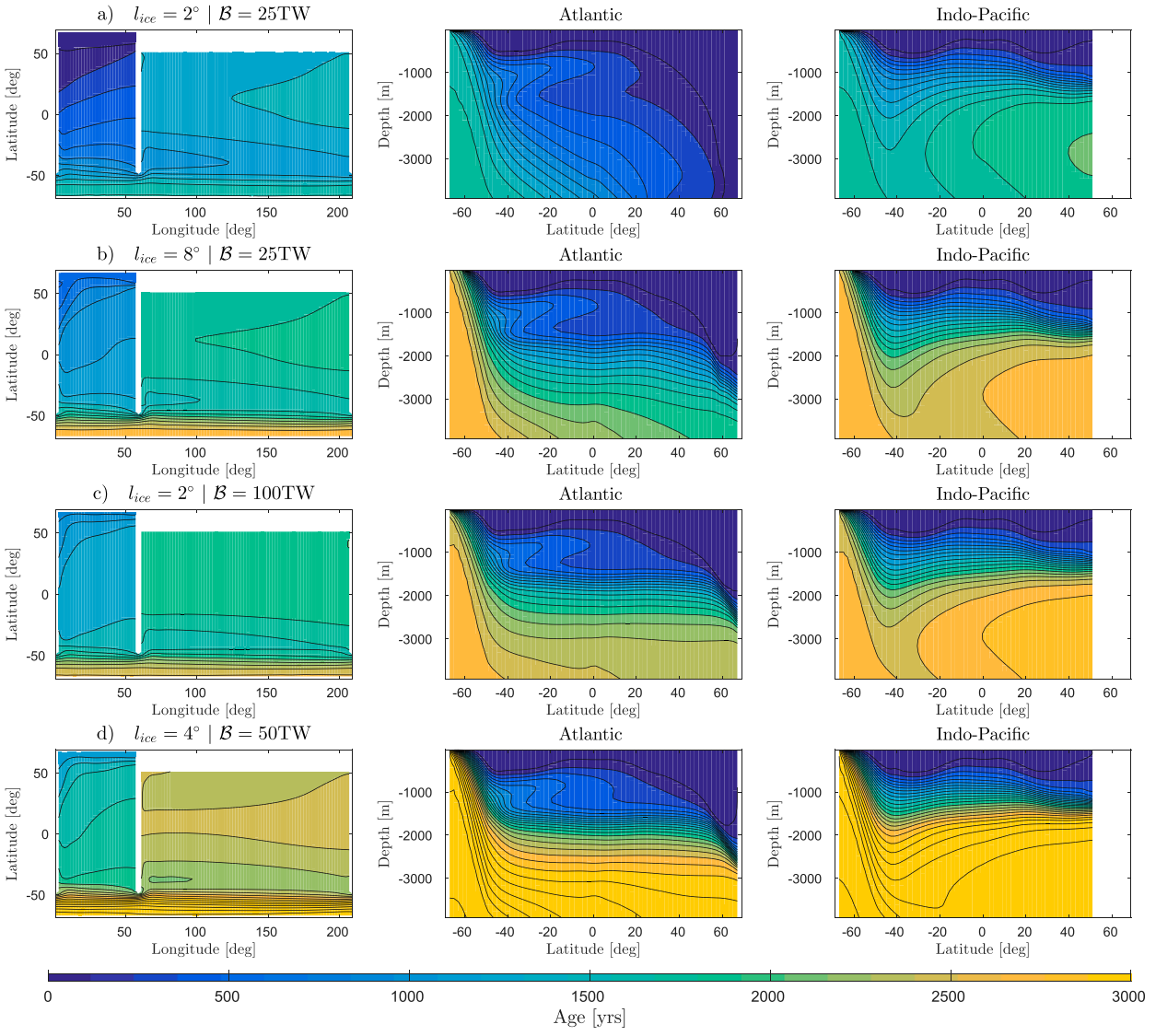

FIG. 5. Age tracer obtained considering a no-flux boundary condition under the ice strips for (a) the reference case, (b) quadrupling l_{ice}, (c) quadrupling $\mathcal{B}$, and (d) doubling l_{ice} and $\mathcal{B}$. (left) Depth-averaged age tracer. (center),(right) Zonally averaged age in the Atlantic and Indo-Pacific basins, respectively. Contour interval is 150 years.

different simulations. If the sea ice acts as a perfect lid (no-flux boundary condition under ice strips), an expansion of the ice strips significantly increases tracer ages at depth in both basins (second row of Fig. 5). The average age in the lower half of the water column A_{abyss} increases from 1400 years in the reference case to 2200 years when $l_{\text{ice}} = 8°$. A similar ''aging'' is observed for an increase in surface buoyancy flux (third row of Fig. 5) where $A_{\text{abyss}} = 2400$ years. This confirms the key role of the shoaling of the middepth MOC cell in isolating the water mass of the abyssal cell from those above. In addition to the average age increase, the shoaling of the middepth cell results in a substantial reduction of the latitudinal age gradient in the lower half of the water column—this reduction is the result of the expansion of the lower cell in the abyssal Atlantic (Fig. 4). For reasons we do not fully understand, the age of the abyssal water masses becomes even older ($A_{\text{abyss}} = 3100$ years) in the simulation more representative of a glacial climate with a simultaneous increase of l_{ice} and $\mathcal{B}$.

The age results are quite different if the age tracer is restored to zero under the ice strips to represent a brittle sea ice cover permeable to air–sea fluxes. Figure 6 shows that in this limit the average age in the lower half of the water column increases only marginally from 600 years in the reference simulation to 800 years in the simulation with $\mathcal{B} = 100$ TW and actually decreases to 500 years in the simulation with $l_{\text{ice}} = 8°$. The age decrease with increased

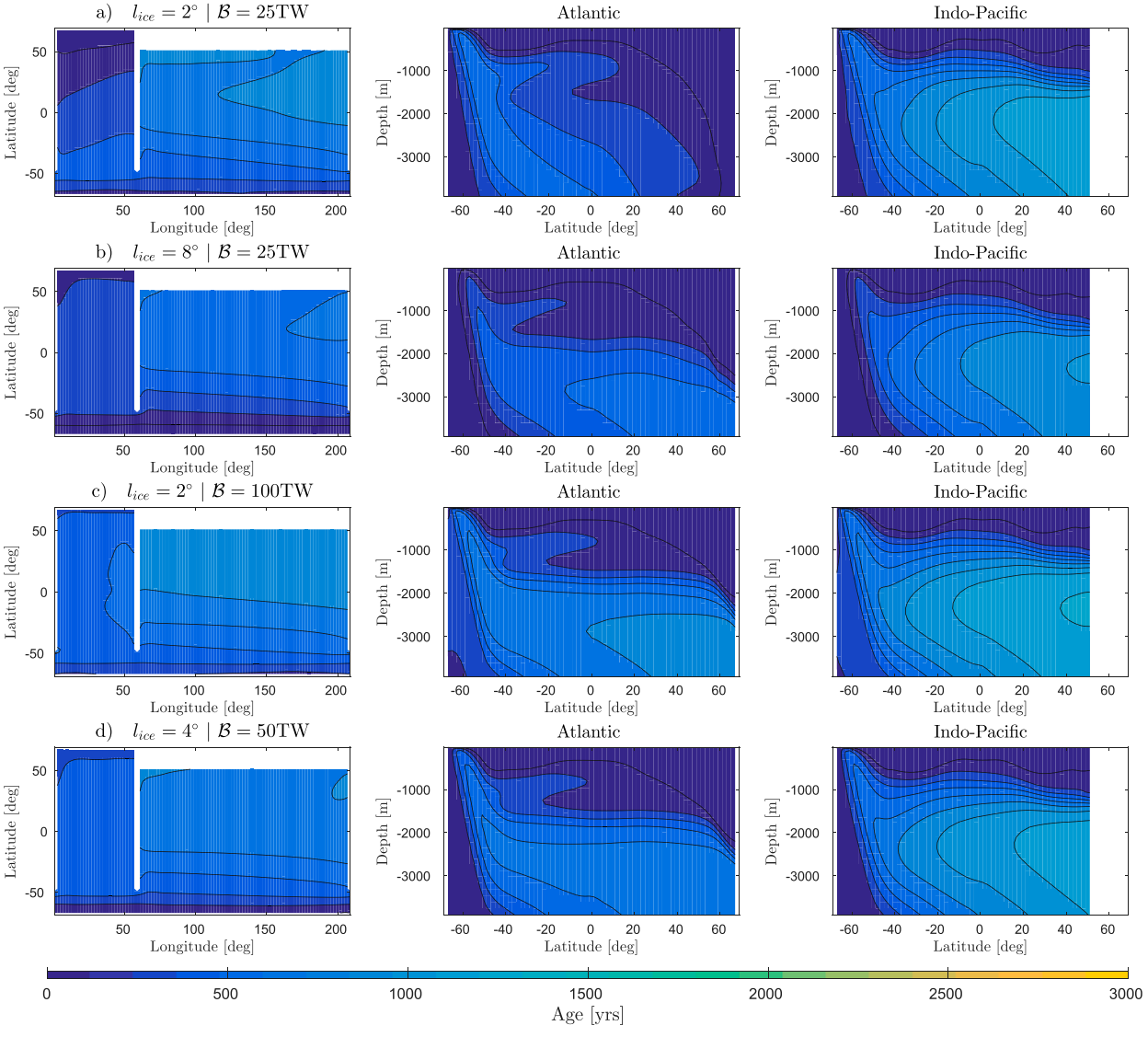

FIG. 6. As in Fig. 5, but using ice strips that are permeable to atmosphere–ocean exchanges (age tracer restored to zero everywhere at the surface). Contour interval is 150 years.

l_{ice} may appear somewhat counterintuitive, but it is consistent with the fact that as l_{ice} increases so does the area where abyssal waters are subject to surface age restoring.

These results suggest that shoaling NADW alone is not sufficient to drive a significant reduction in abyssal ventilation. A reduction in ventilation requires the shielding effect of an insulating sea ice cover around Antarctica to suppress air–sea exchanges with the atmosphere during the formation of abyssal waters. If water mass ages are reset to zero around Antarctica, their ages are set by the overturning time scale of the lower cell (Watson et al. 2015) and are independent of the topology of the circulation. However if waters are shielded from the atmosphere when they upwell under sea ice, then their ages depend on the rate at which the middepth and abyssal cells exchange waters and hence on the connection between the two cells through circulation pathways or mixing.

Ages of water masses in the real ocean can be inferred from the distribution of radiocarbon. Radiocarbon is not produced in the ocean interior and decays at a known rate, and thus satisfies an equation similar to the ideal age tracer. However the surface restoring time scale of ocean radiocarbon is about 10 years. If the residency time of waters at the surface is much longer than 10 years, then radiocarbon behaves much like an age tracer with a zero restoring time scale (ages are reset to zero when waters come to the surface). If waters spend less than 10 years at the surface, radiocarbon behaves more like an age tracer with a no-flux surface boundary

condition (infinite restoring time scale). Focusing on the ventilation of deep waters at high latitudes, waters that sink in the North Atlantic spend a long time at the surface in the subpolar gyres before sinking and thus their radiocarbon ages are restored to the atmospheric values, while waters that sink in the Southern Ocean spend less time at the surface and thus their surface boundary condition is somewhat intermediate between a zero and an infinite restoring time scale (Gebbie and Huybers 2012). A comparison of our simulations with recent radiocarbon estimates confirms that the bulk structure of ocean radiocarbon ages lies somewhere in between that of our two age tracers. For example, radiocarbon estimates for the LGM Pacific middepth age maximum are around 2800 years (e.g., Skinner et al. 2017), while in our cold-climate simulation with $l_{ice} = 4°$ and $\mathcal{B} = 50$ TW, the Pacific middepth age maximum is about 4000 years when using the no-flux condition and about 1300 years when using the zero-age restoring condition. A middepth age maximum has also been inferred from LGM radiocarbon ages (e.g., Burke et al. 2015). A middepth maximum is reproduced in our cold-climate simulation only when the age tracer is restored to zero under the ice strips, suggesting that the no-flux boundary condition overestimates the insulating effect of sea ice. Radiocarbon age distributions seem to sit between those of our two age tracers also for the present day. Radiocarbon ages display little variations with latitude around Antarctica (e.g., Gebbie and Huybers 2012), while in our reference simulation the age tracer in the channel increases toward the south with the no-flux condition, but decreases toward the south with the flux condition.

Our numerical results would seem to be inconsistent with those of Schmittner (2003), who computed radiocarbon ages in present-day and LGM simulations using a realistic sea ice cover distribution that limited air–sea exchanges as a function of sea ice concentration. Schmittner (2003) observed an increase in radiocarbon ages on the order of only 100 years for the LGM-type simulation. However, their simulations were tuned to have similar NADW depths both in the present-day and LGM simulations. This was done to investigate changes in ventilation associated with the increase in sea ice surface alone, without changes in circulation. Here, we demonstrate that it is crucial to consider the strong connection between the sea ice extent and changes in the MOC to properly capture the variations in ventilation rate of the abyss.

6. Role of vertical mixing

Finally we consider the role of vertical mixing on the ventilation of the abyss. For a no-flux boundary condition under ice, we claimed that the water masses of the middepth cell can be isolated from those of the abyssal cell when the isopycnal separating the two cells moves upward into a region of weak mixing. Thus, a vertical profile with strong uniform mixing in the entire water column is predicted to prevent any separation between the two cells. On the other hand, a weak uniform mixing should enhance the isolation of abyssal waters. To test this hypothesis, we repeat the same experiments as in the previous section using a no-flux boundary condition below the ice strips, but using weak ($\kappa_v = 10^{-5}$ m^2 s^{-1}) and strong ($\kappa_v = 10^{-4}$ m^2 s^{-1}) constant-mixing profiles in the entire water column. Tracer ages obtained from this set of simulations are shown in Fig. 7. To separate the effect of vertical mixing on passive tracers from its effect on the overturning circulation, we only modify the model's age tracer diffusivity. Overturning circulations from this new set of experiments are thus identical to those shown in Fig. 4. For presentation purpose, we show the age tracer zonally averaged over both basins.

Figure 7b shows results from the same simulation used for Fig. 5 with the reference κ_v profile shown in Fig. 2. As discussed in the previous section, the average age in the lower half of the water column increases from 1400 years in the reference present-day experiment to 3100 years when l_{ice} and $\mathcal{B}$ are both doubled. As expected, the abyssal age decreases when a strong mixing is used in the entire water column (Fig. 7a): A_{abyss} increases from 700 years in the reference experiment to only 1100 years in the doubled l_{ice} and $\mathcal{B}$ experiment. In contrast, abyssal water becomes more isolated when a weak mixing is used in the entire water column (Fig. 7c): A_{abyss} increases from 1600 to 4300 years for a doubling of l_{ice} and $\mathcal{B}$. These results confirm that variations in the ventilation of the abyss are strongly modulated by the vertical mixing profile. In summary, three ingredients are needed to obtain a very old abyssal water mass: 1) little or no overlap (and hence advective exchange) between the middepth and abyssal cell, 2) little or no surface ventilation of abyssal-cell waters outcropping under sea ice around Antarctica, and 3) weak diffusive exchange at the cell interface. If any of these conditions is not met, the respective process limits water mass ages in the abyssal cell.

7. Discussion

Using a series of idealized simulations, we demonstrated that the depth at which NADW flows toward the Southern Ocean is affected by the negative buoyancy flux under permanent sea ice around Antarctica through two mechanisms: (i) the latitudinal extent of the sea ice cover and (ii) the magnitude of the flux under the sea ice, which is supposed to represent a change in sea ice formation rate. Both the increase in latitudinal extent and formation rate of sea ice, expected in glacial climates, resulted

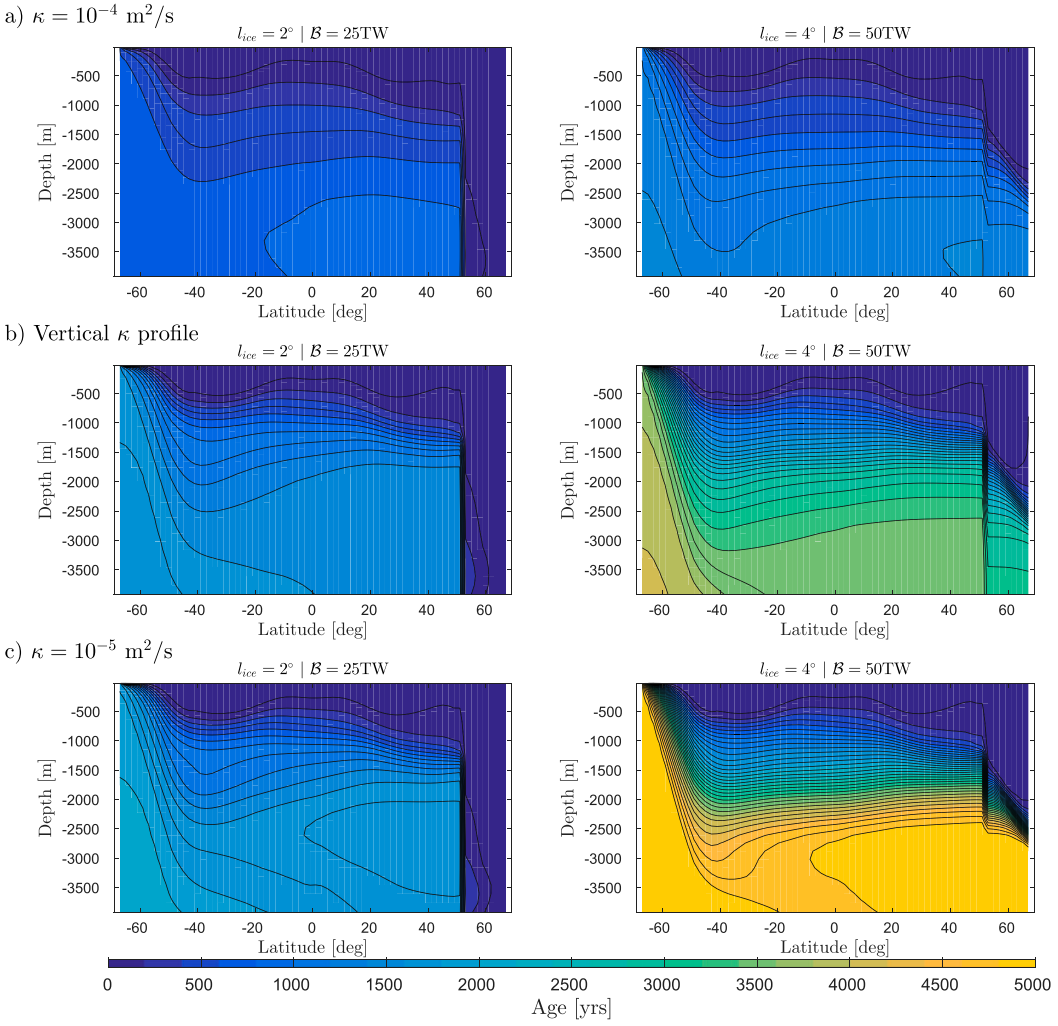

FIG. 7. Globally averaged age tracer obtained considering a no-flux boundary condition under the ice strips for different age tracer diffusivity profiles: (a) $\kappa_v = 10^{-4}\,\mathrm{m^2\,s^{-1}}$, (b) κ_v profile increasing with depth, and (c) $\kappa_v = 10^{-5}\,\mathrm{m^2\,s^{-1}}$. Results for (left) the reference experiment and (right) an experiment with combined increased l_{ice} and $\mathcal{B}$. Contour interval is 150 years.

in a shoaling of NADW and a significant reduction in the overlap and exchange of water masses between the two middepth and abyssal meridional overturning circulations.

Several aspects of the ocean physics are omitted in our idealized setup such as the use of a linear equation of state depending only on temperature, a highly simplified representation of the impact of sea ice through a fixed surface buoyancy flux, a flat bottom ocean, fixed winds, and fixed vertical and isopycnal eddy diffusivities. The influence of these additional physics on the ocean circulation in different climates will need to be addressed in future studies. But our goal here was not to provide the most comprehensive description of the circulation in glacial climates. Rather we focused on one aspect of the problem that is clearly relevant and whose impact could be thoroughly understood and quantified, namely the role of buoyancy loss around Antarctica on the depth of NADW. We believe that our approach provides useful insights that are hard to extract from complex models.

An important question for studies of glacial climates is whether the shoaling of NADW is associated with an aging of abyssal water masses. We considered two idealized age tracers, one being restored to zero at the surface regardless of the presence of sea ice, and the other satisfying a no-flux boundary condition under sea ice, to represent thick sea ice impermeable to air–sea fluxes. In cold climates, simulated through either an increase of sea ice latitudinal extent and/or formation rate, the shoaling of NADW resulted in a significant increase of the age of abyssal water masses only if the age tracer satisfied the no-flux boundary conditions under sea ice. This suggests that a significant aging of abyssal water masses requires a thick layer of permanent sea ice around Antarctica.

These results shed new important insights on the role played by the ocean in the carbon budget of glacial climates. It is believed that the ocean stored much of the carbon leaving the atmosphere during ice ages (e.g., Broecker 1991; Sigman and Boyle 2000; Sigman et al. 2010). Two main mechanisms have been proposed for explaining this carbon uptake. Stephens and Keeling (2000) argued that excess carbon was trapped under the expanding Antarctic sea ice. This argument fell somewhat out of favor when it was pointed out that much of the sea ice around Antarctica melts in summer opening a large window for air–sea carbon fluxes. Our work shows that the criticism no longer applies, once it is recognized that the abyssal overturning cell is fed by waters that come to the surface only in regions of net surface buoyancy loss, which in turn appear to be associated with permanent sea ice cover (Ferrari et al. 2014; Abernathey et al. 2016). When the permanent sea ice expands and its formation rate increases, NADW shoals and the abyssal overturning cell becomes progressively more isolated from the mid-depth one. If the sea ice is *thick* and prevents air–sea fluxes, then abyssal waters become very old, consistent with proxy data (e.g., Skinner et al. 2017), and can potentially store large amounts of carbon for a long time.

An alternative scenario has been suggested, where the uptake of carbon during glacial climates is driven by an increase in the efficiency of the surface biological productivity around Antarctica [see the reviews by Sigman and Boyle (2000) and Sigman et al. (2010)]. This would require sea ice to be sufficiently *thin* or polynyas to form often enough to permit photosynthesis by allowing air–sea fluxes of oxygen and carbon and penetration of light in the surface mixed layer. In this limit the carbon pump can become more efficient through an expansion of the area of the abyssal cell exposed to the surface (Watson et al. 2015) or an increase in the aeolian deposition of iron-rich dust (Mahowald et al. 1999). However, this limit would also likely allow for a relatively efficient reset of radiocarbon ages at the surface around Antarctica, making it harder to explain the observed increase in deep-ocean radiocarbon ages (e.g., Skinner et al. 2017).

The literature on glacial climates often invokes multiple mechanisms to account for the large drawdown of atmospheric carbon by the ocean (e.g., Brovkin et al. 2007). While our framework is too idealized to quantify the role of specific mechanisms, it illustrates which ones may have worked together and which ones may instead not be compatible. In particular we find that a thick ice scenario is consistent with both $\Delta^{14}C$ depleted abyssal waters and increased ocean carbon concentrations, but may not be consistent with increased biological productivity. Conversely a thin ice scenario cannot account for the aging of abyssal water masses. These inferences demonstrate the value of idealized studies like this one, where physics is added one piece at a time, to provide insight on the interaction between the various components of the climate system.

Acknowledgments. L.P.N. acknowledges support from NSERC and FRQNT. M.F.J. and RF acknowledge support through NSF awards OCE-1536515 and OCE-1736109. The MITgcm and the configuration files for the reference simulation discussed in this study are available online (https://github.com/MITgcm/MITgcm; https://bitbucket.org/lpnadeau/antarctic-sea-ice-control-on-the-nadw/src/master/).

REFERENCES

Abernathey, R. P., I. Cerovecki, P. R. Holland, E. Newsom, M. Mazloff, and L. D. Talley, 2016: Water-mass transformation by sea ice in the upper branch of the Southern Ocean overturning. *Nat. Geosci.*, **9**, 596–601, https://doi.org/10.1038/ngeo2749.

Adkins, J. F., 2013: The role of deep ocean circulation in setting glacial climates. *Paleoceanogr. Paleoclimatol.*, **28**, 539–561, https://doi.org/10.1002/palo.20046.

——, K. McIntyre, and D. Schrag, 2002: The salinity, temperature and $\delta^{18}O$ content of the glacial deep ocean. *Science*, **298**, 1769–1773, https://doi.org/10.1126/science.1076252.

Anderson, R. F., S. Ali, L. I. Bradtmiller, S. H. H. Nielsen, M. Q. Fleisher, B. E. Anderson, and L. H. Burckle, 2009: Wind-driven upwelling in the Southern Ocean and the deglacial rise in atmospheric CO_2. *Science*, **323**, 1443–1448, https://doi.org/10.1126/science.1167441.

Balwada, D., K. G. Speer, J. H. LaCasce, W. B. Owens, J. Marshall, and R. Ferrari, 2016: Circulation and stirring in the southeast Pacific Ocean and the Scotia Sea sectors of the Antarctic circumpolar current. *J. Phys. Oceanogr.*, **46**, 2005–2027, https://doi.org/10.1175/JPO-D-15-0207.1.

Broecker, W. S., 1982: Ocean chemistry during glacial time. *Geochim. Cosmochim. Acta*, **46**, 1689–1705, https://doi.org/10.1016/0016-7037(82)90110-7.

——, 1991: The great ocean conveyor. *Oceanography*, **4** (2), 79–89, https://doi.org/10.5670/oceanog.1991.07.

Brovkin, V., A. Ganopolski, D. Archer, and S. Rahmstorf, 2007: Lowering of glacial atmospheric CO_2 in response to changes in oceanic circulation and marine biogeochemistry. *Paleoceanogr. Paleoclimatol.*, **22**, PA4202, https://doi.org/10.1029/2006PA001380.

Burke, A., A. L. Stewart, J. F. Adkins, R. Ferrari, M. F. Jansen, and A. F. Thompson, 2015: The glacial mid-depth radiocarbon bulge and its implications for the overturning circulation. *Paleoceanogr. Paleoclimatol.*, **30**, 1021–1039, https://doi.org/10.1002/2015PA002778.

Curry, W., and D. Oppo, 2005: Glacial water mass geometry and the distribution of $\delta^{13}C$ of ΣCO_2 in the western Atlantic Ocean. *Paleoceanogr. Paleoclimatol.*, **20**, PA1017, https://doi.org/10.1029/2004PA001021.

de Boer, A. M., D. M. Sigman, J. R. Toggweiler, and J. L. Russell, 2007: Effect of global ocean temperature change on deep ocean ventilation. *Paleoceanogr. Paleoclimatol.*, **22**, 1944–9186, https://doi.org/10.1029/2005PA001242.

Ferrari, R., M. F. Jansen, J. F. Adkins, A. Burke, A. L. Stewart, and A. F. Thompson, 2014: Antarctic sea ice control on ocean circulation in present and glacial climates. *Proc. Natl. Acad. Sci. USA*, **111**, 8753–8758, https://doi.org/10.1073/pnas.1323922111.

——, L.-P. Nadeau, D. P. Marshall, L. C. Allison, and H. L. Johnson, 2017: A model of the ocean overturning circulation with two closed basins and a reentrant channel. *J. Phys. Oceanogr.*, **47**, 2887–2906, https://doi.org/10.1175/JPO-D-16-0223.1.

Gebbie, G., and P. Huybers, 2012: The mean age of ocean waters inferred from radiocarbon observations: Sensitivity to surface sources and accounting for mixing histories. *J. Phys. Oceanogr.*, **42**, 291–305, https://doi.org/10.1175/JPO-D-11-043.1.

Gent, P. R., and J. C. McWilliams, 1990: Isopycnal mixing in ocean circulation models. *J. Phys. Oceanogr.*, **20**, 150–155, https://doi.org/10.1175/1520-0485(1990)020<0150:IMIOCM>2.0.CO;2.

Gersonde, R., X. Crosta, A. Abelmann, and L. Armand, 2005: Sea-surface temperature and sea ice distribution of the Southern Ocean at the EPILOG Last Glacial Maximum—A circum-Antarctic view based on siliceous microfossil records. *Quat. Sci. Rev.*, **24**, 869–896, https://doi.org/10.1016/j.quascirev.2004.07.015.

Hallberg, R., and A. Gnanadesikan, 2006: The role of eddies in determining the structure and response of the wind-driven Southern Hemisphere overturning: Results from the modeling eddies in the Southern Ocean (meso) project. *J. Phys. Oceanogr.*, **36**, 2232–2252, https://doi.org/10.1175/JPO2980.1.

Jansen, M., 2017: Glacial ocean circulation and stratification explained by reduced atmospheric temperature. *Proc. Natl. Acad. Sci. USA*, **114**, 45–50, https://doi.org/10.1073/pnas.1610438113.

——, and L.-P. Nadeau, 2016: The effect of Southern Ocean surface buoyancy loss on the deep-ocean circulation and stratification. *J. Phys. Oceanogr.*, **46**, 3455–3470, https://doi.org/10.1175/JPO-D-16-0084.1.

Jones, C. S., and P. Cessi, 2016: Interbasin transport of the meridional overturning circulation. *J. Phys. Oceanogr.*, **46**, 1157–1169, https://doi.org/10.1175/JPO-D-15-0197.1.

Liu, Z., S. Shin, R. Webb, W. Lewis, and B. Otto-Bliesner, 2005: Atmospheric CO_2 forcing on glacial thermohaline circulation and climate. *Geophys. Res. Lett.*, **32**, L02706, https://doi.org/10.1029/2004GL021929.

Lumpkin, R., and K. Speer, 2007: Global ocean meridional overturning. *J. Phys. Oceanogr.*, **37**, 2550–2562, https://doi.org/10.1175/JPO3130.1.

Lund, D., J. Adkins, and R. Ferrari, 2011: Abyssal Atlantic circulation during the Last Glacial Maximum: Constraining the ratio between transport and vertical mixing. *Paleoceanogr. Paleoclimatol.*, **26**, PA1213, https://doi.org/10.1029/2010PA001938.

Lynch-Stieglitz, J., and Coauthors, 2007: Atlantic meridional overturning circulation during the Last Glacial Maximum. *Science*, **316**, 66–69, https://doi.org/10.1126/science.1137127.

Mahowald, N., K. Kohfeld, M. Hansson, Y. Balkanski, S. P. Harrison, I. C. Prentice, M. Schulz, and H. Rodhe, 1999: Dust sources and deposition during the Last Glacial Maximum and current climate: A comparison of model results with paleodata from ice cores and marine sediments. *J. Geophys. Res.*, **104**, 15 895–15 916, https://doi.org/10.1029/1999JD900084.

Marshall, J., A. Adcroft, C. Hill, L. Perelman, and C. Heisey, 1997: A finite-volume, incompressible Navier Stokes model for studies of the ocean on parallel computers. *J. Geophys. Res.*, **102**, 5753–5766, https://doi.org/10.1029/96JC02775.

Marzocchi, A., and M. F. Jansen, 2017: Connecting Antarctic sea ice to deep-ocean circulation in modern and glacial climate simulations. *Geophys. Res. Lett.*, **44**, 6286–6295, https://doi.org/10.1002/2017GL073936.

Miller, M. D., M. Simons, J. F. Adkins, and S. E. Minson, 2015: The information content of pore fluid $\delta^{18}O$ and $[Cl-]$. *J. Phys. Oceanogr.*, **45**, 2070–2094, https://doi.org/10.1175/JPO-D-14-0203.1.

Munday, D. R., H. L. Johnson, and D. P. Marshall, 2013: Eddy saturation of equilibrated circumpolar currents. *J. Phys. Oceanogr.*, **43**, 507–532, https://doi.org/10.1175/JPO-D-12-095.1.

Nikurashin, M., and R. Ferrari, 2013: Overturning circulation driven by breaking internal waves in the deep ocean. *Geophys. Res. Lett.*, **40**, 3133–3137, https://doi.org/10.1002/grl.50542.

Roberts, J., and Coauthors, 2016: Evolution of South Atlantic density and chemical stratification across the last deglaciation. *Proc. Natl. Acad. Sci. USA*, **113**, 514–519, https://doi.org/10.1073/pnas.1511252113.

Roche, D. M., X. Crosta, and H. Renssen, 2012: Evaluating Southern Ocean response for the Last Glacial Maximum and pre-industrial climates: PMIP-2 models and data evidence. *Quat. Sci. Rev.*, **56**, 99–106, https://doi.org/10.1016/j.quascirev.2012.09.020.

Roe, P. L., 1986: Characteristic-based schemes for the Euler equations. *Annu. Rev. Fluid Mech.*, **18**, 337–365, https://doi.org/10.1146/annurev.fl.18.010186.002005.

Schmittner, A., 2003: Southern Ocean sea ice and radiocarbon ages of glacial bottom waters. *Earth Planet. Sci. Lett.*, **213**, 52–62, https://doi.org/10.1016/S0012-821X(03)00291-7.

Shin, S.-I., Z. Liu, B. L. Otto-Bliesner, J. E. Kutzbach, and S. J. Vavrus, 2003: Southern Ocean sea-ice control of the glacial North Atlantic thermohaline circulation. *Geophys. Res. Lett.*, **30**, 1096, https://doi.org/10.1029/2002GL015513.

Sigman, D. M., and E. A. Boyle, 2000: Glacial/interglacial variations in atmospheric carbon dioxide. *Nature*, **407**, 859–869, https://doi.org/10.1038/35038000.

——, M. P. Hain, and G. H. Haug, 2010: The polar ocean and glacial cycles in atmospheric CO_2 concentration. *Nature*, **466**, 47–55, https://doi.org/10.1038/nature09149.

Skinner, L. C., and Coauthors, 2017: Radiocarbon constraints on the glacial ocean circulation and its impact on atmospheric CO_2. *Nat. Commun.*, **8**, 16010, https://doi.org/10.1038/ncomms16010.

Stephens, B. B., and R. F. Keeling, 2000: The influence of Antarctic sea ice on glacial-interglacial CO_2 variations. *Nature*, **404**, 171–174, https://doi.org/10.1038/35004556.

Sun, S., I. Eisenman, and A. Stewart, 2016: The influence of Southern Ocean surface buoyancy forcing on glacial-interglacial changes in the global deep ocean stratification. *Geophys. Res. Lett.*, **43**, 8124–8132, https://doi.org/10.1002/2016GL070058.

Talley, L., 2013: Closure of the global overturning circulation through the Indian, Pacific and Southern Oceans: Schematics and transports. *Oceanography*, **26** (1), 80–97, https://doi.org/10.5670/oceanog.2013.07.

Thompson, A. F., A. L. Stewart, and T. Bischoff, 2016: A multi-basin residual-mean model for the global overturning circulation. *J. Phys. Oceanogr.*, **46**, 2583–2604, https://doi.org/10.1175/JPO-D-15-0204.1.

Toggweiler, J. R., 1999: Variation of atmospheric CO_2 by ventilation of the ocean's deepest water. *Paleoceanogr. Paleoclimatol.*, **14**, 571–588, https://doi.org/10.1029/1999PA900033.

——, 2009: Shifting westerlies. *Science*, **323**, 1434–1435, https://doi.org/10.1126/science.1169823.

Watson, A. J., G. K. Vallis, and M. Nikurashin, 2015: Southern Ocean buoyancy forcing of ocean ventilation and glacial atmospheric CO_2. *Nat. Geosci.*, **8**, 861–864, https://doi.org/10.1038/ngeo2538.

Wunsch, C., 2016a: Last Glacial Maximum and deglacial abyssal seawater oxygen isotopic ratios. *Climate Past*, **12**, 1281–1296, https://doi.org/10.5194/cp-12-1281-2016.

——, 2016b: Pore fluids and the LGM ocean salinity—Reconsidered. *Quat. Sci. Rev.*, **135**, 154–170, https://doi.org/10.1016/j.quascirev.2016.01.015.